Journal of Materials Chemistry A

PAPER

View Article Online
View Journal | View Issue

Cite this: J. Mater. Chem. A, 2018, 6, 1682

Nickel metal–organic framework implanted on graphene and incubated to be ultrasmall nickel phosphide nanocrystals acts as a highly efficient water splitting electrocatalyst†

Liting Yan, [a] Huimin Jiang,[a] Yanlong Xing,*[b] Ying Wang, [a] Dandan Liu,[a] Xin Gu, [a] Pengcheng Dai, [a] Liangjun Li [a] and Xuebo Zhao *[a]

The development of low-cost, efficient, and stable electrocatalysts with bifunctional catalytic activity for overall water splitting is desirable but remains a great challenge. Here, a template-confinement strategy is presented with nickel metal–organic framework (MOF-74-Ni) implanted on graphene oxide and incubated by low temperature phosphorization to become ultrasmall nickel phosphide nanocrystals anchored on reduced graphene oxide (termed Ni_2P/rGO). The size-controlled synthesis of ultrasmall metal-based catalysts is of vital economic interest and scientific importance for chemical conversion technologies. The Ni_2P/rGO guarantees large active surface area and perfect dispersity of the active sites with ultrasmall particle sizes (average about 2.6 nm), which can serve as a highly efficient electrocatalyst for overall water splitting. In 1.0 M KOH, the Ni_2P/rGO exhibited remarkable electrocatalytic performance for both HER and OER, affording a current density of 10 mA cm^{-2} at overpotentials of 142 mV for HER and 260 mV for OER with small Tafel slope. Furthermore, an electrolyzer employed with Ni_2P/rGO as a bifunctional catalyst in both the cathode and anode in 1.0 M KOH generated 10 mA cm^{-2} at a voltage of 1.61 V with excellent stability, comparable to the integrated Pt/C and RuO_2 counterparts, which is among the best performances of transition metal phosphides (TMPs).

Received 20th November 2017
Accepted 20th December 2017

DOI: 10.1039/c7ta10218f

rsc.li/materials-a

1. Introduction

Electrolysis of water, a sustainable technology that generates H_2 and O_2 *via* hydrogen evolution reaction (HER) and oxygen evolution reaction (OER), has attracted extensive attention due to its environmentally friendly properties and potential for large-scale commercialization.[1–5] However, because of the reaction kinetics of the two core redox processes for water splitting, both the OER and HER need high overpotentials for activation, which greatly limits the practical applications of overall water splitting.[2] Currently, precious metal Pt-based materials and Ir/Ru-based materials are state-of-the-art catalysts for HER and OER respectively, but their high cost, low natural abundance and unsatisfactory durability limit their scale-up applications in industrial deployment.[6,7] Over the past decade, enormous effort and progress have been made to develop efficient, stable and noble metal-free alternative electrocatalysts, such as transition metal sulfides,[8–10] selenides,[11–13] phosphides,[14–18] and other transition metal-based composites.[19–23]

Among the aforementioned materials, transition metal phosphides (TMPs, *e.g.*, $Ni_{12}P_5$,[24] Ni_2P,[25,26] Ni_5P_4,[27] Cu_3P,[28] CoP,[17] FeP,[29] MoP[30]) have emerged as the most promising HER catalysts due to their hydrogenase-like catalytic mechanism and high catalytic activity and durability.[14,31] In addition, theoretical calculations show that Ni_2P possesses superior activity over the noble metal catalysts for HER, implying the synthesis of Ni_2P is of great significance in both theory and practice.[25,32,33] Furthermore, Hu *et al.* first showed that Ni_2P was also highly active for OER.[34] Using Ni_2P as a catalyst for OER has drawn particular attention and achieved excellent electrocatalytic performance,[4,35–37] suggesting the potential of Ni_2P as a bifunctional electrocatalyst for overall water splitting.

[a]Research Centre of New Energy Science and Technology, Research Institute of Unconventional Oil & Gas and Renewable Energy, China University of Petroleum (East China), Qingdao 266580, P. R. China. E-mail: zhaoxuebo@upc.edu.cn

[b]Leibniz Institute for Analytical Sciences, Berlin 12489, Germany. E-mail: yanlong.xing@isas.de

† Electronic supplementary information (ESI) available: Experimental section, PXRD patterns and SEM images of MOF-74-Ni and MOF-74-Ni/GO, XPS survey spectra and elemental mappings of the Ni_2P/rGO, high-resolution XPS spectra in the C 1s region of MOF-74-Ni/GO and Ni_2P/rGO, TEM images of MOF-74-Ni/GO, PXRD patterns of Ni_2P/C and Ni_2P particles, electrochemical cyclic voltammetry curves at different potential scanning rates, N_2 adsorption–desorption isotherm, LSV of Ni_2P/rGO before and after the pre-activation process, high-resolution XPS spectra in the Ni 2p region of Ni_2P/rGO after the pre-activation process and 2000 CVs, PXRD patterns and additional TEM images of Ni_2P/rGO after the pre-activation process, LSV of Ni_2P/rGO/NF for OER and HER, ICP results, summary of various TMPs catalysts for OER and HER, summary of various catalytic electrodes for overall water splitting. See DOI: 10.1039/c7ta10218f

To achieve high catalytic activity, various strategies have been developed, such as optimized nanostructures, porous structures with high Brunauer–Emmett–Teller (BET) surface area and high dispersion of active sites on highly conductive supports (porous carbon, graphene, carbon nanotubes, *etc.*). To a great extent, reducing the sizes of metal-based particles, especially synthesis of ultrasmall nanoclusters or even single atoms, would be an effective way to improve catalytic performance.[38–40] However, the preparation of Ni_2P combined with multiple favorable factors still remains a challenging task.

Recently, metal–organic frameworks (MOFs) have been proven to be ideal precursors to synthesize a variety of porous nanostructured carbon/metal composites with perfect dispersity of active sites;[25,41,42] MOF-derived carbon-confined metal species have gained growing interest and achieved excellent electrocatalytic performance.[36,43–46] The metal derivatives and graphitized/amorphous carbon matrix derived from the metal centers and organic ligands of MOF precursors can function as catalytic active sites and electron highways, respectively, during the catalytic process. The uniform dispersion of metallic active sites and the coordination effect in the MOF precursors ensure that the metal source aggregates, making the intrinsic electronic and surface composition of MOF-derivatives different from the surface coating of the active sites at the surface/interface, which favors the catalytic performance.[38,47] Lou *et al.* reported that MOF-derived porous nickel phosphide nanoplates manifest excellent electrocatalytic activity for OER in alkaline solutions.[36] In our previous work, we fabricated hierarchically porous Ni_2P polyhedrons *via* an *in situ* conversion strategy of one-step calcination at low temperature, which showed impressive electrocatalytic activity in basic solutions.[25] Mai *et al.* reported nickel phosphide supported on graphene was remarkably active and a stable OER catalyst in alkaline media, and ascribed improved OER performance to the introduction of graphene.[35] Despite the achieved superior progress of half-cell reactions, there are few reports on developing effective electrocatalysts for both OER and HER in the same electrolyte based on a single catalyst to achieve the overall water splitting.[48–50] Therefore, the development of highly efficient bifunctional electrocatalysts for overall water splitting is of prime importance.[50,51]

Herein, nickel metal–organic frameworks (MOF-74-Ni) implanted on graphene oxide and incubated with phosphorization to become ultrasmall nickel phosphide nanocrystals anchored on reduced graphene oxide (termed as Ni_2P/rGO) are reported as highly efficient bifunctional electrocatalysts for overall water splitting. The MOF-74-Ni/graphene oxide (termed as MOF-74-Ni/GO) was synthesized *via* a facile one-step room-temperature reaction and the Ni_2P/rGO was obtained after a one-step calcination at low temperature with sodium hypophosphite as a phosphorus source (Scheme 1). The Ni_2P/rGO guaranteed large active surface areas and perfect dispersity of the active sites with ultrasmall particle sizes (average about 2.6 nm). In addition, due to the specific interfacial effect between MOF and graphene oxide, the carbon/graphene surface tends to form homogeneous carbon during the phosphorization calcinations, which could connect into a carbon network and function as an electron highway to obtain satisfactory electronic conductivity and enhanced charge-transfer efficiency. As a result, the Ni_2P/rGO exhibited excellent catalytic performance for both HER and OER in 1.0 M KOH. Furthermore, an electrolyzer employing Ni_2P/rGO as a bifunctional catalyst in both the cathode and anode generated 10 mA cm^{-2} at a voltage of 1.61 V with excellent stability, which is comparable to the integrated Pt/C and RuO_2 counterparts and among the best performances of TMPs.

2. Experimental

2.1 Synthesis of MOF-74-Ni nanocrystals

MOF-74-Ni was prepared from a modified procedure.[52] In a typical procedure, 2,5-dihydroxyterephthalic acid (DHTA, 0.991 g, 5 mmol) and sodium hydroxide (0.800 g, 20 mmol) were mixed in 100 mL distilled water; then, nickel acetate tetrahydrate (2.488 g, 10 mmol) was dissolved in another 50 mL distilled water. After vigorous stirring for 0.5 hour at room temperature, the two solutions were mixed in a beaker with a volume of 250 mL. After vigorous stirring for another 0.5 hour, the beaker was sealed with sealing film and continuously stirred for another 24 hours at room temperature. Then the fine faint yellow crystalline product was recovered by centrifugation and washed several times with distilled water. Finally, the yellow crystals were obtained by vacuum freeze drying for 12 h.

2.2 Synthesis of MOF-74-Ni/GO hybrid composites

MOF-74-Ni/GO hybrid composites were synthesized using a similar procedure to that of MOF-74-Ni described above, except for the addition of GO aqueous solution (5 wt% of nickel acetate tetrahydrate).

2.3 Synthesis of Ni_2P/rGO, Ni_2P particles and Ni_2P/C hybrid composites

In a typical procedure, 50 mg as-prepared MOF-74-Ni/GO and 1.0 g $NaH_2PO_2 \cdot H_2O$ were placed in two separate positions in a typical corundum porcelain boat with MOF-74-Ni/GO at the downstream position. The samples were heated at 275 °C for three hours (5 °C min^{-1}) under a constant flow of nitrogen at 30 mL min^{-1}. After naturally cooling to ambient temperature, ultrasmall Ni_2P/rGO nanocrystals were obtained. Ni_2P particles and MOF-derived Ni_2P carbon composites (termed as Ni_2P/C) were synthesized using a similar procedure to that described above, except for the use of nickel acetate tetrahydrate and MOF-74-Ni as the nickel source.[25]

2.4 Characterization and electrochemical measurements

The phases of the materials were confirmed using powder X-ray diffraction patterns (PXRD, PANalytical X'pert PRO). The scanning electron microscopy (SEM) and transmission electron microscopy (TEM) images of as-prepared catalysts were recorded on JSM-7500F microscope and JEOL JEM2100F microscope, respectively. X-ray photoelectron spectra (XPS, Thermo ESCALAB 250, Al Kα) were conducted to obtain the elemental composition and chemical state of the materials. The elemental

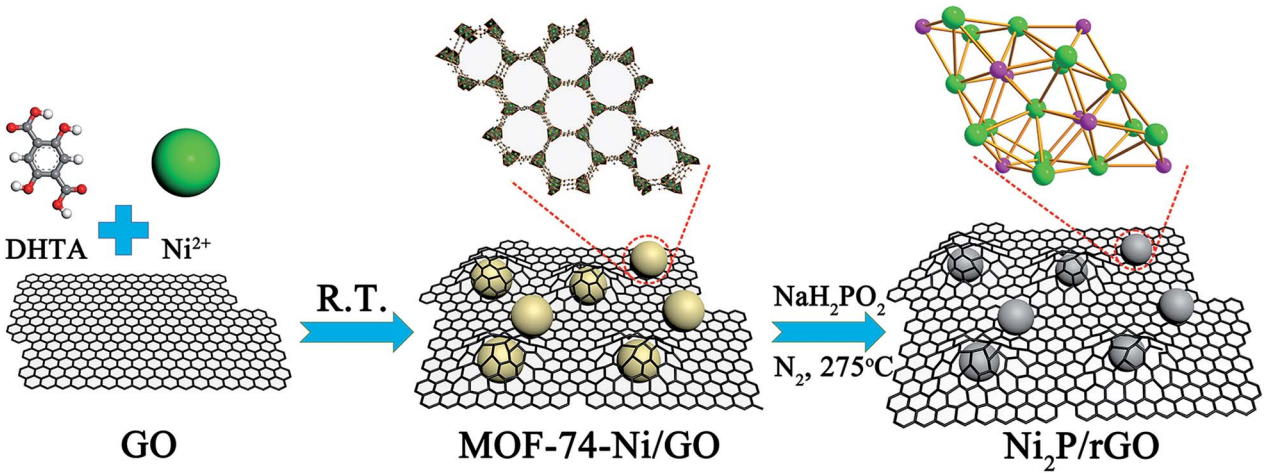

Scheme 1 Illustration of the synthesis procedure for the Ni_2P/rGO.

contents of the materials were characterized using inductively coupled plasma analysis (ICP, Vista Axial, USA). Raman spectra were recorded using JY HR800 under ambient conditions. N_2 adsorption–desorption experiments were carried out on an Autosorb-iQ_2 (Quantachrome Instruments, USA) instrument.

All the electrochemical experiments were conducted on the electrochemical workstation (CHI 760E) in a three-electrode system in 1.0 M KOH solution at room temperature, with the glassy carbon electrode (GCE, 0.071 cm^2 in area), Ag/AgCl and Pt wire/carbon rod as the working electrode, reference electrode and the counter electrode, respectively. Five milligram catalysts were dispersed in 1 mL of ethanol/distilled water/Nafion (v/v/v = 9 : 9 : 2) and followed by a sonication process of 30 min to obtain the suspension liquid. Then, 3.5 μL well-dispersed catalysts (about 0.25 mg cm^{-2}) were placed on the GCE with drying at 60 °C for the test. Linear sweep voltammetry (LSV, 5 mV s^{-1}) and continuous cyclic voltammetry (CV, 100 mV s^{-1}) scans were recorded to characterize the polarization curves and the long-term stability, respectively. The time-dependent current density (*i*–*t*) curve was obtained at 260 mV (*vs.* RHE) for OER and −142 mV (*vs.* RHE) for HER. All potentials were referenced to a reversible hydrogen electrode (RHE) with *iR* correction: $E_{vs.RHE} = E_{vs.Ag/AgCl} + 0.197 + 0.05916pH\text{-}iR$, where the *R* refers to the ohmic resistance, which could be obtained from the electrochemical impedance spectroscopy (EIS).

3. Results and discussion

3.1 Material preparation and characterization

The proposed strategy to synthesize ultrasmall nickel phosphide nanocrystals anchored on reduced graphene oxide (Ni_2P/rGO) is illustrated in Scheme 1. MOF-74-Ni supported on graphene oxide (MOF-74-Ni/GO) was first synthesized *via* a facile reaction at ambient temperature. Then the obtained MOF-74-Ni/GO was phosphorized into Ni_2P/rGO, as outlined in our previous report, with sodium hypophosphite as a phosphorus source, and is shown in detail in the ESI.†[25] For comparison, nonporous Ni_2P particles (obtained using nickel acetate tetrahydrate as the nickel source) and MOF-derived Ni_2P carbon composites (termed as Ni_2P/C, obtained using MOF-74-Ni as the nickel source) were prepared according to our previous work with small modifications (see details in ESI†).[25] Powder X-ray diffraction (PXRD) patterns indicated that the MOF-74-Ni and MOF-74-Ni/GO nanocrystals had similar patterns as the reference (Fig. S1†), indicating the successful synthesis of the MOF precursor.[52,53] In addition, the PXRD patterns (Fig. S2†) confirmed the successful preparation of Ni_2P particles and Ni_2P/C. Scanning electron microscopy (SEM) photos showed that MOF-74-Ni nanocrystals of 20–80 nm size (Fig. S3a†) grew uniformly on the surface of GO (Fig. S3b and c†) due to a coordination effect between Ni^{2+} and oxygen species on the surface of GO, clearly indicating the template-directed effect of GO.[54] After the low-temperature phosphorization calcinations, Ni_2P/rGO was obtained. The PXRD patterns of Ni_2P/rGO (Fig. 1)

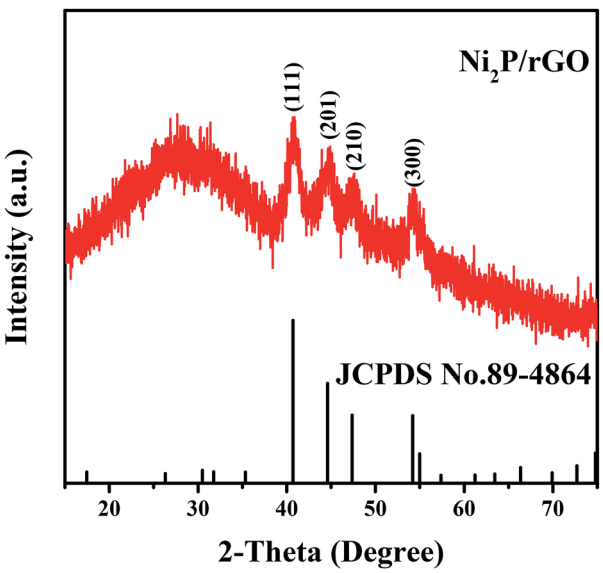

Fig. 1 PXRD patterns of Ni_2P/rGO.

show four typical peaks at $2\theta = 40.7°$, 44.6°, 47.4° and 54.2°, which can be assigned to the (111), (201), (210) and (300) planes of Ni_2P (JCPDS no. 89-4864), respectively. Based on the Scherrer formula, the average crystallite sizes of Ni_2P were obtained. The corresponding crystallite sizes calculated from the peak widths of the PXRD pattern were 10.49 nm, 8.55 nm, 9.67 nm and 11.75 nm, respectively. Furthermore, the broad diffraction peak appearing at around 25° can be assigned to the (002) plane of disorderedly stacked graphene sheets, suggesting the successful reduction of graphene oxide to its reduced phase during the phosphorization calcinations.[55,56]

To confirm the elemental composition and chemical state of Ni_2P/rGO, X-ray photoelectron spectroscopy (XPS) spectra were obtained. The XPS survey spectra (Fig. S4†) of Ni_2P/rGO confirmed the presence of Ni, P, C and O, which further illustrated the formation of Ni_2P on rGO. Fig. 2a and b show the high-resolution C 1s XPS spectra of MOF-74-Ni/GO and Ni_2P/rGO. The C 1s peaks observed at 284.8, 286.2 and 289.1 eV can be assigned to carbon in the form of C–C, C–O and O═C–O, respectively. Despite the C 1s of Ni_2P/rGO showing similar oxygen-containing functionalities, the intensities of O═C–O at 289.1 eV (Fig. 2a and b and S5†) were much smaller than those in MOF-74-Ni/GO, confirming the successful reduction of GO to rGO, and the domination of C–C which could function as an electron highway to obtain satisfactory electronic conductivity and enhanced charge-transfer efficiency.[4,45,55] In the high-resolution XPS spectrum (Fig. 2c), the characteristic peaks of Ni 2p at 853.4 and 871.3 eV could be assigned to the Ni $2p_{3/2}$ and $2p_{1/2}$ energy levels of $Ni^{\delta+}$ in Ni_2P, which is in accordance with literature reports.[36,37,57,58] Similarly, the peaks at 857 and 876 eV corresponded to the Ni $2p_{3/2}$ and $2p_{1/2}$ energy levels of Ni^{2+} in NiO, respectively, which can be attributed to the inescapable air exposure. Fig. 2d shows the high-resolution P 2p XPS spectrum of Ni_2P/rGO. Correspondingly, the P species at 129.9 eV can be assigned to P $2p_{3/2}$ in Ni_2P, while the peaks at around 133.9 eV represent oxidized P species arising from superficial oxidation.[36,45,59,60] The XPS results clearly confirm the successful synthesis of Ni_2P/rGO after the low-temperature phosphorization calcinations, in accordance with the PXRD patterns in Fig. 1.

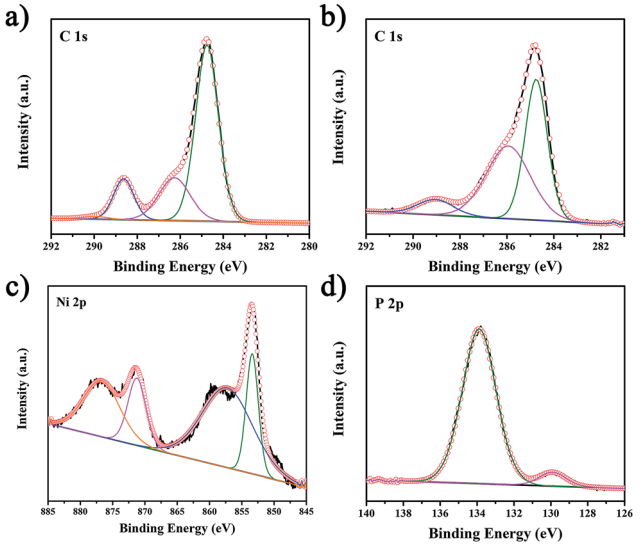

Fig. 2 (a) High-resolution C 1s XPS spectra of the MOF-74-Ni/GO. (b) High-resolution C 1s XPS spectra of the Ni_2P/rGO. (c) High-resolution Ni 2p XPS spectra of the Ni_2P/rGO. (d) High-resolution P 2p XPS spectra of the Ni_2P/rGO.

Fig. 3a and b and S6† show the low and high magnification SEM images of Ni_2P/rGO derived from MOF-74-Ni/GO. It can be seen that Ni_2P/rGO exhibits similar sheet-like structures as its MOF precursor, indicating the *in situ* transformation from MOF to Ni_2P in accordance with our previous work.[25] Also, the exposed defects of rGO sheets on the Ni_2P/rGO demonstrated that the ultrasmall nickel phosphide nanocrystals are grown on both surfaces of rGO to give a sandwich-type structure of Ni_2P/rGO. The element mapping (Fig. S7†) confirms that P, Ni and C were uniformly distributed throughout the Ni_2P/rGO. To obtain more information about the inner microstructure of the prepared Ni_2P/rGO, the composites were further characterized by transmission electron microscopy (TEM). Low-resolution TEM images (Fig. 3c) show that Ni_2P/rGO remained in the initial shape of the starting MOF-74-Ni/GO (see TEM images in Fig. S8†) and crystals uniformly distributed on the rGO surface without agglomeration. From the high-resolution TEM (HRTEM) image (Fig. 3d), the Ni_2P nanocrystals were anchored uniformly on the carbon/graphene surface with an average size of about 2.6 nm, and the Ni loading determined by ICP was 19.8 wt% (Table S1†). Because of the specific interfacial effect between MOF and graphene oxide, the carbon/graphene surface (Fig. 3d and f) tends to form homogeneous carbon during the phosphorization calcinations, which could connect into a carbon network and function as an electron highway to obtain satisfactory electronic conductivity and enhanced charge-transfer efficiency. Furthermore, the small interatomic distance between Ni and C atoms in MOF-74-Ni could enable the incorporation of Ni_2P on the surface of rGO by means of the homogeneous carbon during the phosphorization process. In addition, the coordination effect in the MOF precursors confines the metal source to aggregate at the same time, inducing the formation of ultrasmall nickel phosphide nanocrystals. The intrinsic electronic and surface composition of MOF-derivatives are different from the surface coating of the active sites at the surface/interface, which favors the catalytic performance. The Raman spectrum (Fig. S9†) of Ni_2P/rGO exhibits two prominent peaks at 1367 and 1550 cm^{-1}, corresponding to D band and G band of the carbon materials, confirming the existence of rGO nanosheet.[35,61–63] A broad D peak further confirms rGO with a high degree of graphitization. Moreover, there are no obvious Raman peaks related to Ni_2P/C, as reported in other work.[54] In addition, the particle size distribution is demonstrated in Fig. 3e, which shows that all Ni_2P nanocrystals had a size between 1.6 nm and 3.7 nm with an average size of about 2.6 nm, which was similar to the average crystallite sizes calculated from the PXRD pattern (~10 nm). Fig. 3f shows well-resolved lattice fringes with a distance of approximately 0.221 nm, corresponding to the (111) plane of Ni_2P and proving the formation of Ni_2P on the surface of graphene.

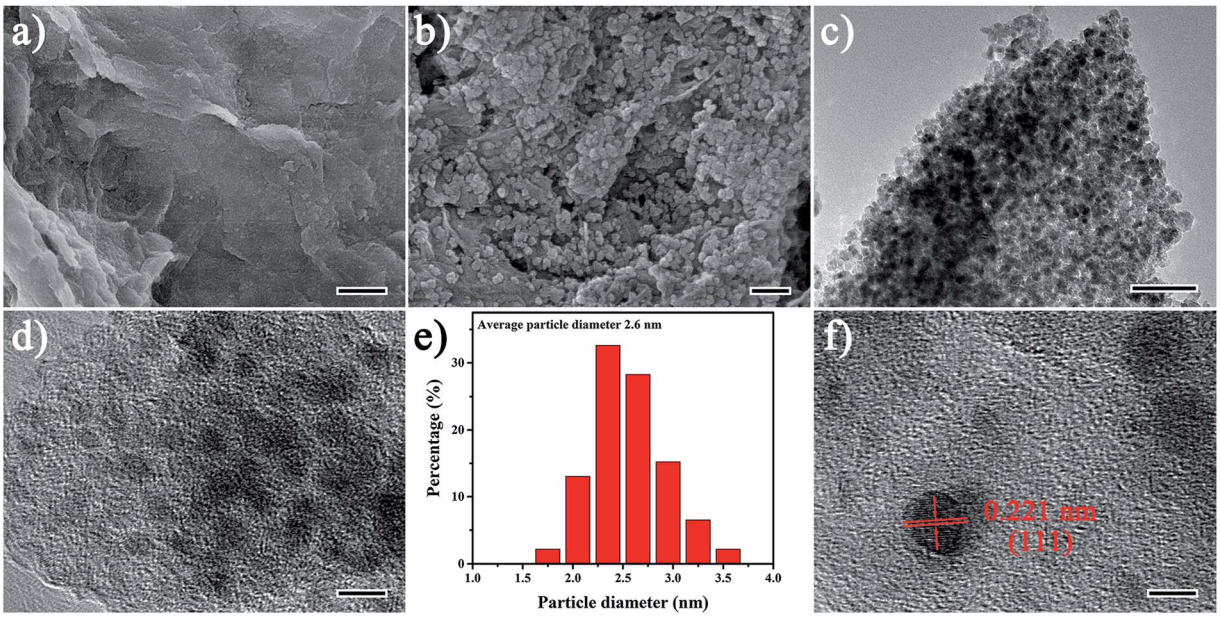

Fig. 3 (a) Low and (b) high magnification SEM images of Ni_2P/rGO. (c) TEM images of Ni_2P/rGO, (d) TEM images and (e) corresponding size distribution pattern of Ni_2P/rGO. (f) HRTEM images of Ni_2P/rGO. Scale bars (a) 1 μm, (b) 100 nm, (c) 50 nm, (d) 5 nm, and (f) 5 nm.

3.2 Characterization of electrocatalytic performance

Due to the high activation barrier and the sluggish four proton-coupled electron transfer, the reaction kinetics of the OER at the anode were the major bottleneck of the electrochemical water splitting.[4,64,65] Thus, the electrocatalytic performance of Ni_2P/rGO toward OER was first evaluated using a standard three-electrode system in an alkaline electrolyte (1.0 M KOH). Before recording the OER performance, all the prepared samples were pre-treated with 20 cyclic voltammetry (CV) cycles with scan rates of 100 mV s^{-1} as the pre-activation process. All the data are presented with *iR*-correction. For comparison, bare GCE, rGO, Ni_2P particles, Ni_2P/C and commercially available standardized RuO_2 catalysts were also examined under the same conditions. Fig. 4a shows the polarization curves of the as-prepared catalyst obtained by linear sweep voltammetry (LSV) measurements. Among the above catalysts, Ni_2P/rGO exhibited the best electrocatalytic performance with the same overpotentials for OER. The operational overpotential of Ni_2P/rGO to deliver a current density of 10 mA cm^{-2} was as low as 260 mV, considerably smaller than that of Ni_2P particles (355 mV), Ni_2P/C (275 mV), RuO_2 (280 mV), and many other non-precious metal-based electrocatalysts as well (Table S2†).

The electrocatalytic kinetics involved in the OER of Ni_2P/rGO, Ni_2P/C, Ni_2P particles and RuO_2 were examined by corresponding Tafel plots, as shown in Fig. 4b. As expected, the Tafel slope of Ni_2P/rGO was about 62 mV dec^{-1}, which was the smallest of the three typical Ni_2P catalysts and commercial RuO_2, indicating the favorable OER kinetics of Ni_2P/rGO. Furthermore, the exchange current density (i_0) of as-prepared catalysts was obtained based on the Butler–Volmer electrochemical kinetic model.[66–69] The i_0 of Ni_2P/rGO was calculated to be 2.4×10^{-5} A cm^{-2}, obviously higher than that of Ni_2P/C (1.2×10^{-5} A cm^{-2}) and Ni_2P particles (1.3×10^{-6} A cm^{-2}), indicating the superior catalytic efficiency of Ni_2P/rGO. To gain insight into the intrinsic activity of the as-prepared catalysts, the turnover frequencies (TOFs) of three Ni_2P electrocatalysts were then measured according to a previously described method (details included in the ESI†).[70] The TOF values of Ni_2P/rGO, Ni_2P/C and Ni_2P particles calculated at the overpotential of 300 mV were 0.074 s^{-1}, 0.035 s^{-1} and 0.0064 s^{-1}, respectively, further confirming the higher intrinsic catalytic activity of Ni_2P/rGO.

To gain more insights into the possible origin of the high electrocatalytic performance of Ni_2P/rGO, the electrode kinetics/interface reactions and the electrochemical active surface areas (ECSAs) were investigated. The electrochemical impedance spectroscopy (EIS) was obtained at a potential of 1.53 V (*vs.* RHE) to study the electrode kinetics and interfacial properties. As shown in Fig. 4c, the R_s mainly resulted from the ohmic resistance of the solution and the contact at the interface of the electrode/electrolyte. The small values of R_s (about 1.6 Ω) corresponded to the close contact between the current collector and catalysts, which could accelerate electrical integration and promote the electrocatalytic performance of electrocatalysts. Furthermore, the charge transfer resistance (R_{ct}) of Ni_2P/rGO (31.8 Ω) was lower than that of Ni_2P/C (36.3 Ω) and Ni_2P particles (58.1 Ω), which means faster charge transfer kinetics of Ni_2P/rGO, suggesting that electrical conductivity had been enhanced due to the doping of graphene.[71,72] The ECSAs were estimated using the electrochemical double-layer capacitance (C_{dl}) for further insight into the different catalytic performances. Compared to the EIS which correlated with the efficiency of charge transfer, the capacitive current could reflect charge accumulation rather than chemical reactions or charge transfer.[11] Fig. 4d shows that the calculated C_{dl} values (calculated from corresponding CVs with multiple scan rates, Fig. S10†) of Ni_2P/rGO, Ni_2P/C and Ni_2P particles were 71.7 mF cm^{-2},

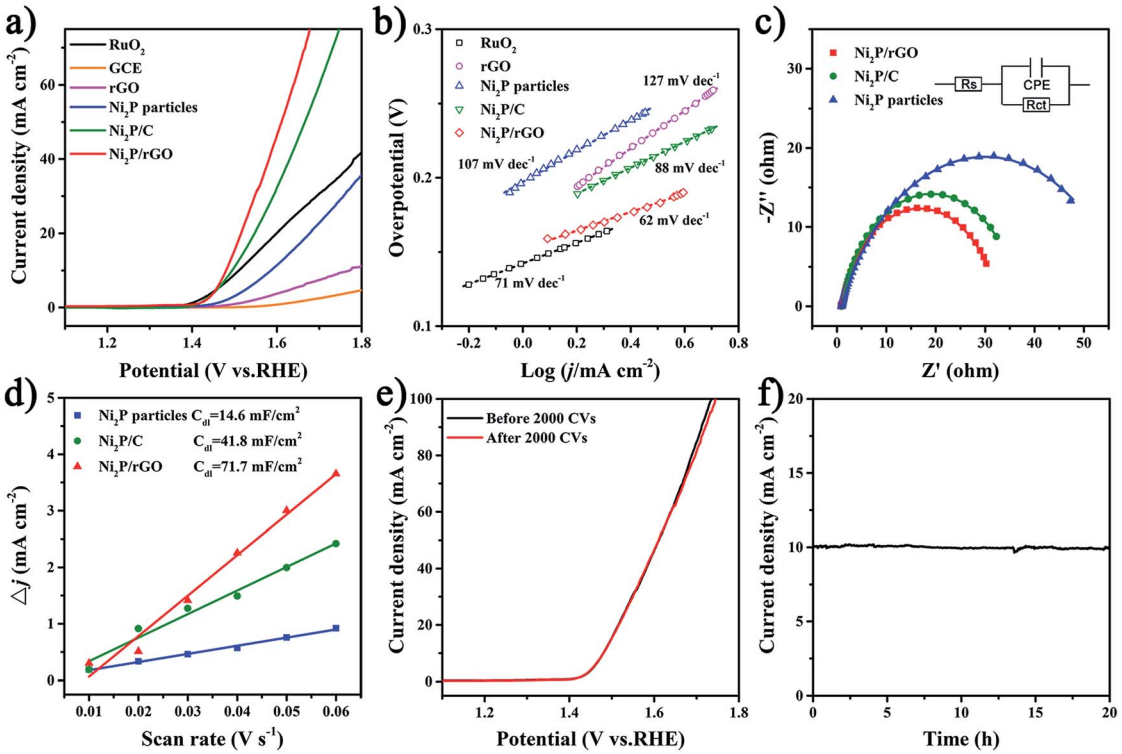

Fig. 4 (a) OER polarization curves of as-prepared catalysts. (b) OER Tafel plots obtained from the OER polarization curves. (c) EIS Nyquist plots of as-prepared catalysts, (d) Plots of the capacitive currents as a function of scan rate of as-prepared catalysts. (e) OER polarization curves of Ni_2P/rGO before and after 2000 CV cycles. (f) The current–time curves of Ni_2P/rGO in 1.0 M KOH.

41.8 mF cm^{-2} and 14.6 mF cm^{-2}, respectively, corresponding to the ECSA values of 84.4 cm^2, 49.2 cm^2 and 17.2 cm^2. The higher C_{dl} and ECSA values of Ni_2P/rGO indicated that higher electrocatalytic activity of the Ni_2P/rGO could partly come from the large surface area, attributed to the optimized unique porous nanostructures, larger BET surface area (70.0 m^2 g^{-1}, Fig. S11†) and high dispersion of ultrasmall Ni_2P active sites anchored on graphene. Furthermore, the Ni loading of Ni_2P/rGO (19.8 wt%, Table S1†) was much smaller than that of Ni_2P/C (28.5 wt%) and Ni_2P particles (47.6 wt%), implying the high utilization ratio of the ultrasmall Ni_2P anchored on graphene.

The superior durability of the electrocatalyst is another major issue for practical application in energy conversion systems. Therefore, continuous CV scanning of the Ni_2P/rGO was conducted in the potential range 1.0–1.6 V (*vs.* RHE) with a scan rate of 100 mV s^{-1} in 1.0 M KOH solution. As can be seen in Fig. 4e, the OER activity remained almost unchanged after 2000 CVs, suggesting the excellent stability of the Ni_2P/rGO. In addition, the long-term electrochemical durability of the Ni_2P/rGO was tested using time-dependent current density (*i*–*t*) curve. Fig. 4f shows that the current density had no significant decrease after 20 h testing, indicating the superior long-term durability of the Ni_2P/rGO.

To further understand the origin of the superior OER activity and durability, PXRD, TEM and XPS characterizations of the Ni_2P/rGO after the pre-activation process and post-OER in alkaline electrolyte solution were performed. Interestingly, the first scan had a predominant broad peroxidation peak before the onset potential that diminished after the pre-activation process (Fig. S12†). A similar observation was reported for Ni_2P, CoP and Co_2P, signifying the irreversible oxidation of metal centers in many TMPs-based electrocatalysts.[34,36,73,74] In attempt to further confirm the composition change on the surface, XPS and HRTEM of the Ni_2P/rGO after the pre-activation process were performed. After the pre-activation process, the characteristic peak at 853.6 eV at the energy level of Ni $2p_{3/2}$ corresponds to the $Ni^{\delta+}$ in Ni_2P, confirming the retention of Ni_2P after pre-activation process. Furthermore, a peak at around 856.1 eV observed in the Ni $2p_{3/2}$ spectrum and the corresponding satellite peak at 861.8 eV (Fig. S13†) could be attributed to $Ni(OH)_2$ or NiOOH species formed during the oxygen evolution reaction as reported.[34,35,75,76] Since $Ni(OH)_2$ could be oxidized into NiOOH during the oxygen evolution reaction,[77] these peaks could be attributed to characteristic peaks of NiOOH, which was further proved by HRTEM results. In the TEM images (Fig. S14†), ultrasmall nanocrystals of Ni_2P were uniformly embedded on the surface of rGO as before the pre-activation process. In addition, HRTEM of Ni_2P/rGO (Fig. S15†) after the pre-activation process showed well-resolved lattice fringes with interplanar distances of 0.221 and 0.254 nm, which could be attributed to (111) and (200) planes of Ni_2P, respectively. In addition, the PXRD patterns (Fig. S16†) showed that there was no obvious change of phase for Ni_2P/rGO, which was in accordance with the HRTEM results. Lattice spacings of 0.241 nm and 0.239 nm presented in the image were assigned to the (011) plane of NiOOH and (111)

plane of NiO, respectively, indicating the fabrication of Ni_2P/NiOH/NiO_x core–shell heterostructure on the surface/interface during the OER. These results were consistent with the XPS results. Positive-shifted Ni centers and negative-shifted P centers could function as hydroxyl/hydride-acceptor and proton-acceptor centers for OER/HER, which is in favour of the adsorption–desorption process of the reactant and resultant molecules; the enhanced local electric dipole resulting from the electrons' diffusion from Ni to P will lower the energy barrier of the electrocatalytic process.[4,67,78–80] Furthermore, the carbon/graphene network serving as an electron pathway could continuously and effectively ensure electron transport, while the ultrasmall Ni_2P/NiOH/NiO_x core–shell heterostructure served as the electrocatalytic active sites, resulting in highly efficient OER/HER performance. From the above, the synergistic effect of all the favorable factors creates the improvement of the electrocatalytic performance. Moreover, the comparison of the XPS of Ni_2P/rGO after the pre-activation process and after 2000 CVs (Fig. S17†) OER showed little difference, confirming that the Ni_2P/NiOH/NiO_x core–shell heterostructure was mainly fabricated during the pre-activation process. This could account for the excellent durability of Ni_2P/rGO after the pre-activation process.

Furthermore, the HER activities of the as-prepared electrocatalysts were also evaluated in 1.0 M KOH to explore their potential for the overall water splitting. Fig. 5a shows that the Ni_2P/rGO exhibited a low overpotential of 142 mV to obtain the current density of 10 mA cm^{-2}, which was smaller than those of Ni_2P/C (185 mV), Ni_2P particles (310 mV) and many other non-precious metal-based electrocatalysts (Table S3†). The electrocatalytic kinetics involved in the HER of Ni_2P/rGO, Ni_2P/C, Ni_2P particles and Pt/C were obtained using corresponding Tafel plots (Fig. 5b). Notably, the Tafel slope of 58 mV dec^{-1} for Ni_2P/rGO was much smaller than those of Ni_2P/C (75 mV dec^{-1}) and Ni_2P particles (104 mV dec^{-1}), and the i_0 of Ni_2P/rGO was calculated to be 3.1×10^{-5} A cm^{-2}, obviously higher than that of Ni_2P/C (1.7×10^{-5} A cm^{-2}) and Ni_2P particles (7.8×10^{-6} A cm^{-2}), implying favourable electrochemical reaction kinetics of the Ni_2P/rGO. In addition, continuous CV scanning (Fig. 5c) and the 20 h *i–t* curve (Fig. 5d) of the electrocatalysts indicated that the Ni_2P/rGO presented excellent durability in alkaline solutions. Using 0.5 M H_2SO_4 (pH = 0) and 1.0 M PBS (pH = 7) solutions as electrolyte, the OER and HER catalytic performance of Ni_2P/rGO in acidic and neutral media was assessed to confirm the intrinsic catalytic activity of Ni_2P/rGO. The Ni_2P/rGO performs with similar catalytic activity in both acidic and neutral media (Fig. S18†). Also, the low Tafel plots indicate fast electrocatalytic kinetics of Ni_2P/rGO in acidic and neutral media. The satisfactory electrocatalytic performance of Ni_2P/rGO could be attributed to highly active Ni_2P centers and excellent conductive carbon/graphene network.

Inspired by the satisfactory OER and HER performance of the Ni_2P/rGO bifunctional electrocatalysts in the alkaline solutions, a two-electrode electrolyzer was assembled using the deposition of Ni_2P/rGO onto conductive nickel foam substrates as both the anode and cathode (Ni_2P/rGO/NF||Ni_2P/rGO/NF) to assess its catalytic activity for overall water splitting in 1.0 M KOH. For

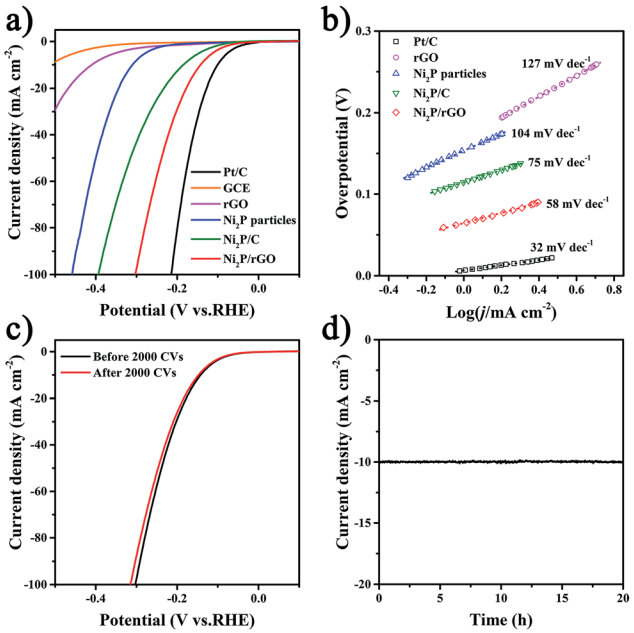

Fig. 5 (a) HER polarization curves of as-prepared catalysts. (b) HER Tafel plots obtained from the HER polarization curves. (c) HER polarization curves of Ni_2P/rGO before and after 2000 CV cycles. (d) The current–time curve of Ni_2P/rGO in 1.0 M KOH.

comparison, Ni_2P/C/NF and Ni_2P particles/NF as both the anode and cathode were also evaluated. Impressively, nickel foam substrates showed slight OER and HER performance, but the deposition of Ni_2P/rGO onto NF further enhanced its electrocatalytic performance, with a lower overpotential of 250 mV at 10 mA cm^{-2} for OER and 115 mV for HER (Fig. S19†). In comparison with Ni_2P/rGO/GCE substrates, the enhanced electrocatalytic activity of Ni_2P/rGO/NF substrates could be attributed to the excellent conductivity and electron transfer ability of the NF, which could provide a synergistic effect with Ni_2P/rGO catalyst during the electrocatalytic process.[81] In order to find out the appropriate catalyst loading, the specific activity of Ni_2P/rGO with different mass loading was calculated on the basis of previous reports.[82] Fig. S20† shows that with the increase of mass loading, the catalytic performance of Ni_2P/rGO remarkably increased, suggesting the high-activity of Ni_2P/rGO catalysts, while the values of specific activity calculated at the overpotential of 300 mV were 2.5×10^{-3} mA cm^{-2} (0.5 mg cm^{-2}), 2.9×10^{-3} mA cm^{-2} (1.0 mg cm^{-2}), 1.8×10^{-3} mA cm^{-2} (2.0 mg cm^{-2}), 1.1×10^{-3} mA cm^{-2} (4.0 mg cm^{-2}) and 0.7×10^{-3} mA cm^{-2} (8.0 mg cm^{-2}). The best specific activity of Ni_2P/rGO with the mass loading of 1.0 mg cm^{-2} means the highest ratio of performance to price of Ni_2P/rGO catalysts, so the overall water splitting performance was evaluated at this mass loading. As is illustrated in Fig. 6a, the Ni_2P/rGO delivered a current density of 10 mA cm^{-2} at a cell voltage of 1.61 V in 1.0 M KOH electrolyte solution, which was lower than that of Ni_2P/C (1.63 V), Ni_2P particles (1.66 V) and many other non-precious metal-based electrocatalysts (Table S4†). This is comparable to that of the benchmark precious metal-based catalysts Pt/C||RuO_2, which deliver a current density of 10 mA cm^{-2} at 1.60 V, but inferior to

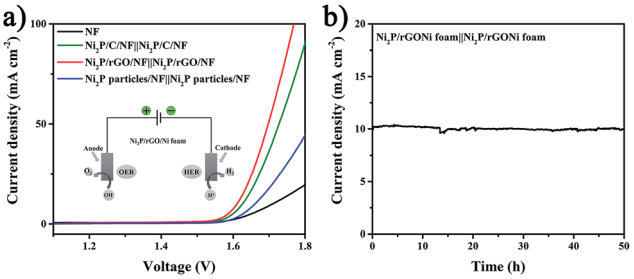

Fig. 6 (a) The overall water splitting performance of the as-prepared catalysts (inset: the schematic diagram for overall water splitting reaction in a two-electrode configuration). (b) The catalytic stability of the Ni_2P/rGO/NF in 1.0 M KOH.

the Ni_2P/rGO after 1.62 V (Fig. S21†).[4,83,84] More importantly, the Ni_2P/rGO/NF||Ni_2P/rGO/NF couple also showed superior durability (Fig. 6b) in the overall water splitting reaction with negligible current density loss after 50 h of continuous electrolysis, suggesting its practical applications as a new type of electrocatalyst for overall water splitting.

4. Conclusions

In summary, we report a novel template-confinement strategy with nickel metal–organic framework (MOF-74-Ni) implanted on graphene oxide and incubated to become ultrasmall nickel phosphide nanocrystals anchored on reduced graphene oxide (termed as Ni_2P/rGO). Due to the specific interfacial effect between MOF and graphene oxide, as well as the small interatomic distance between Ni and C atoms in MOF-74-Ni, the obtained Ni_2P/rGO possesses large active surface areas, a homogeneous carbon network and perfect dispersity of active sites with ultrasmall particle sizes (average about 2.6 nm). Profiting from the Ni_2P/NiOH/NiO_x core–shell heterostructure formed during the pre-activation process, the Ni_2P/rGO showed remarkable electrocatalytic performance for both HER and OER in an alkaline electrolyte. Furthermore, our electrolyzer employed Ni_2P/rGO as both the cathode and anode in 1.0 M KOH generating 10 mA cm^{-2} at a voltage of 1.61 V with excellent stability, which is comparable to the integrated Pt/C and RuO_2 counterparts, and is among the best performance of transition metal phosphides (TMPs). Additionally, the Ni_2P/rGO presented impressive long-term durability. Our synthesis strategy presents important guidelines for the rational design and accurate modulation of various metal-based nanomaterials for energy-related applications.

Conflicts of interest

There are no conflicts to declare.

Acknowledgements

This work was supported by the National Natural Science Foundation of China (Grant No. 21473254), the Special Project Fund of "Taishan Scholar" of Shandong Province (Grant No. ts201511017), the Natural Science Foundation of Shandong Province (Grant No. ZR2017BB059), and the Fundamental Research Funds for the Central Universities (Grant No. 17CX02038A).

Notes and references

1 Y. Jia, L. Zhang, G. Gao, H. Chen, B. Wang, J. Zhou, M. T. Soo, M. Hong, X. Yan, G. Qian, J. Zou, A. Du and X. Yao, *Adv. Mater.*, 2017, **29**, 1700017.
2 T. Tang, W.-J. Jiang, S. Niu, N. Liu, H. Luo, Y.-Y. Chen, S.-F. Jin, F. Gao, L.-J. Wan and J.-S. Hu, *J. Am. Chem. Soc.*, 2017, **139**, 8320–8328.
3 Y. Pi, Q. Shao, P. Wang, J. Guo and X. Huang, *Adv. Funct. Mater.*, 2017, **27**, 1700886.
4 L. Yan, L. Cao, P. Dai, X. Gu, D. Liu, L. Li, Y. Wang and X. Zhao, *Adv. Funct. Mater.*, 2017, **27**, 1703455.
5 H. Duan, D. Li, Y. Tang, Y. He, S. Ji, R. Wang, H. Lv, P. P. Lopes, A. P. Paulikas, H. Li, S. X. Mao, C. Wang, N. M. Markovic, J. Li, V. R. Stamenkovic and Y. Li, *J. Am. Chem. Soc.*, 2017, **139**, 5494–5502.
6 B. Rausch, M. D. Symes, G. Chisholm and L. Cronin, *Science*, 2014, **345**, 1326–1330.
7 Y. Jiao, Y. Zheng, M. Jaroniec and S. Z. Qiao, *Chem. Soc. Rev.*, 2015, **44**, 2060–2086.
8 B. Ma, P. Y. Guan, Q. Y. Li, M. Zhang and S. Q. Zang, *ACS Appl. Mater. Interfaces*, 2016, **8**, 26794–26800.
9 C. Wu, J. Maier and Y. Yu, *Adv. Mater.*, 2016, **28**, 174.
10 Q. Wang, R. Zou, W. Xia, J. Ma, B. Qiu, A. Mahmood, R. Zhao, Y. Yang, D. Xia and Q. Xu, *Small*, 2015, **11**, 2511–2517.
11 A. T. Swesi, J. Masud and M. Nath, *Energy Environ. Sci.*, 2016, **9**, 1771–1782.
12 X. Wang, F. Li, W. Li, W. Gao, Y. Tang and R. Li, *J. Mater. Chem. A*, 2017, **5**, 17982–17989.
13 C. Xia, Q. Jiang, C. Zhao, M. N. Hedhili and H. N. Alshareef, *Adv. Mater.*, 2016, **28**, 77–85.
14 M. Sun, H. Liu, J. Qu and J. Li, *Adv. Energy Mater.*, 2016, **6**, 1600087.
15 Y. Zhang, Y. Liu, M. Ma, X. Ren, Z. Liu, G. Du, A. M. Asiri and X. Sun, *Chem. Commun.*, 2017, **53**, 11048–11051.
16 Y. Sun, L. Hang, Q. Shen, T. Zhang, H. Li, X. Zhang, X. Lyu and Y. Li, *Nanoscale*, 2017, **9**, 16674–16679.
17 C. Wu, Y. Yang, D. Dong, Y. Zhang and J. Li, *Small*, 2017, **13**, 1602873.
18 M. Zhuang, X. Ou, Y. Dou, L. Zhang, Q. Zhang, R. Wu, Y. Ding, M. Shao and Z. Luo, *Nano Lett.*, 2016, **16**, 4691–4698.
19 H. B. Wu, B. Y. Xia, L. Yu, X.-Y. Yu and X. W. D. Lou, *Nat. Commun.*, 2015, **6**, 6512.
20 L. Fan, P. F. Liu, X. Yan, L. Gu, Z. Z. Yang, H. G. Yang, S. Qiu and X. Yao, *Nat. Commun.*, 2016, **7**, 10667.
21 X. Xu, R. Cao, S. Jeong and J. Cho, *Nano Lett.*, 2012, **12**, 4988–4991.
22 J. Kim, C. Young, J. Lee, Y.-U. Heo, M.-S. Park, M. S. A. Hossain, Y. Yamauchi and J. H. Kim, *J. Mater. Chem. A*, 2017, **5**, 15065–15072.

23 Y. V. Kaneti, J. Zhang, Y.-B. He, Z. Wang, S. Tanaka, M. S. A. Hossain, Z.-Z. Pan, B. Xiang, Q.-H. Yang and Y. Yamauchi, *J. Mater. Chem. A*, 2017, **5**, 15356–15366.
24 Z. Huang, Z. Chen, Z. Chen, C. Lv, H. Meng and C. Zhang, *ACS Nano*, 2014, **8**, 8121–8129.
25 L. Yan, P. Dai, Y. Wang, X. Gu, L. Li, L. Cao and X. Zhao, *ACS Appl. Mater. Interfaces*, 2017, **9**, 11642–11650.
26 B. You, N. Jiang, M. Sheng, M. W. Bhushan and Y. Sun, *ACS Catal.*, 2016, **6**, 714–721.
27 A. Laursen, K. Patraju, M. Whitaker, M. Retuerto, T. Sarkar, N. Yao, K. Ramanujachary, M. Greenblatt and G. C. Dismukes, *Energy Environ. Sci.*, 2015, **8**, 1027–1034.
28 J. Tian, Q. Liu, N. Cheng, A. M. Asiri and X. Sun, *Angew. Chem., Int. Ed.*, 2014, **53**, 9577–9581.
29 X. Zhu, M. Liu, Y. Liu, R. Chen, Z. Nie, J. Li and S. Yao, *J. Mater. Chem. A*, 2016, **4**, 8974–8977.
30 Z. Xing, Q. Liu, A. M. Asiri and X. Sun, *Adv. Mater.*, 2014, **26**, 5702–5707.
31 H. Wang, Y. Xie, H. Cao, Y. Li, L. Li, Z. Xu, X. Wang, N. Xiong and K. Pan, *ChemSusChem*, 2017, **10**, 4899–4908.
32 P. Liu and J. A. Rodriguez, *J. Am. Chem. Soc.*, 2005, **127**, 14871–14878.
33 M. Ledendecker, S. K. Calderon, C. Papp, H.-P. Steinrueck, M. Antonietti and M. Shalom, *Angew. Chem., Int. Ed.*, 2015, **54**, 12361–12365.
34 L.-A. Stern, L. Feng, F. Song and X. Hu, *Energy Environ. Sci.*, 2015, **8**, 2347–2351.
35 M. Wang, M. Lin, J. Li, L. Huang, Z. Zhuang, C. Lin, L. Zhou and L. Mai, *Chem. Commun.*, 2017, **53**, 8372–8375.
36 X.-Y. Yu, Y. Feng, B. Guan, X. W. Lou and U. Paik, *Energy Environ. Sci.*, 2016, **9**, 1246–1250.
37 X. Liang, B. Zheng, L. Chen, J. Zhang, Z. Zhuang and B.-H. Chen, *ACS Appl. Mater. Interfaces*, 2017, **9**, 23222–23229.
38 Y.-T. Xu, X. Xiao, Z.-M. Ye, S. Zhao, R. Shen, C.-T. He, J.-P. Zhang, Y. Li and X.-M. Chen, *J. Am. Chem. Soc.*, 2017, **139**, 5285–5288.
39 X. Kang, H. Liu, M. Hou, X. Sun, H. Han, T. Jiang, Z. Zhang and B. Han, *Angew. Chem.*, 2016, **128**, 1092–1096.
40 E. Roduner, *Chem. Soc. Rev.*, 2006, **35**, 583–592.
41 X. Fang, L. Jiao, R. Zhang and H.-L. Jiang, *ACS Appl. Mater. Interfaces*, 2017, **9**, 23852–23858.
42 Y. V. Kaneti, J. Tang, R. R. Salunkhe, X. Jiang, A. Yu, K. C. W. Wu and Y. Yamauchi, *Adv. Mater.*, 2016, **29**, 1604898.
43 J. Song, C. Zhu, B. Z. Xu, S. Fu, M. H. Engelhard, R. Ye, D. Du, S. P. Beckman and Y. Lin, *Adv. Energy Mater.*, 2016, **7**, 1601555.
44 Y. Xu, W. Tu, B. Zhang, S. Yin, Y. Huang, M. Kraft and R. Xu, *Adv. Mater.*, 2017, **29**, 1605957.
45 P. He, X. Y. Yu and X. W. D. Lou, *Angew. Chem., Int. Ed.*, 2017, **56**, 3897–3900.
46 J. Yang, F. Zhang, X. Wang, D. He, G. Wu, Q. Yang, X. Hong, Y. Wu and Y. Li, *Angew. Chem., Int. Ed.*, 2016, **55**, 12854–12858.
47 S. Ji, Y. Chen, Q. Fu, Y. Chen, J. Dong, W. Chen, Z. Li, Y. Wang, L. Gu, W. He, C. Chen, Q. Peng, Y. Huang, X. Duan, D. Wang, C. Draxl and Y. Li, *J. Am. Chem. Soc.*, 2017, **139**, 9795–9798.
48 Y. Jin, H. Wang, J. Li, X. Yue, Y. Han, P. K. Shen and Y. Cui, *Adv. Mater.*, 2016, **28**, 3785–3790.
49 L.-L. Feng, G. Yu, Y. Wu, G.-D. Li, H. Li, Y. Sun, T. Asefa, W. Chen and X. Zou, *J. Am. Chem. Soc.*, 2015, **137**, 14023–14026.
50 L. Jiao, Y.-X. Zhou and H.-L. Jiang, *Chem. Sci.*, 2016, **7**, 1690–1695.
51 C. Tang, N. Cheng, Z. Pu, W. Xing and X. Sun, *Angew. Chem.*, 2015, **127**, 9483–9487.
52 L. Garzon-Tovar, A. Carne-Sanchez, C. Carbonell, I. Imaz and D. Maspoch, *J. Mater. Chem. A*, 2015, **3**, 20819–20826.
53 P. D. Dietzel, B. Panella, M. Hirscher, R. Blom and H. Fjellvag, *Chem. Commun.*, 2006, 959–961.
54 X. L. Ge, Z. Q. Li and L. W. Yin, *Nano Energy*, 2017, **32**, 117–124.
55 Y. Lu, X. Wang, Y. Mai, J. Xiang, H. Zhang, L. Li, C. Gu, J. Tu and S. X. Mao, *J. Phys. Chem. C*, 2012, **116**, 22217–22225.
56 B. Chen, Y. Meng, F. He, E. Liu, C. Shi, C. He, L. Ma, Q. Li, J. Li and N. Zhao, *Nano Energy*, 2017, **41**, 154–163.
57 L. Han, T. Yu, W. Lei, W. Liu, K. Feng, Y. Ding, G. Jiang, P. Xu and Z. Chen, *J. Mater. Chem. A*, 2017, **5**, 16568–16572.
58 A.-L. Wang, J. Lin, H. Xu, Y.-X. Tong and G.-R. Li, *J. Mater. Chem. A*, 2016, **4**, 16992–16999.
59 C. Tang, L. Xie, K. Wang, G. Du, A. M. Asiri, Y. Luo and X. Sun, *J. Mater. Chem. A*, 2016, **4**, 12407–12410.
60 F. L. Yang, Y. T. Chen, G. Z. Cheng, S. L. Chen and W. Luo, *ACS Catal.*, 2017, **7**, 3824–3831.
61 Z. Li, L. Zhang, X. Ge, C. Li, S. Dong, C. Wang and L. Yin, *Nano Energy*, 2017, **32**, 494–502.
62 K. Zhang, M. Park, J. Zhang, G.-H. Lee, J. Shin and Y.-M. Kang, *Nano Res.*, 2017, 1–14.
63 K. Liu, C.-L. Hsin, D. Fu, J. Suh, S. Tongay, M. Chen, Y. Sun, A. Yan, J. Park, K. M. Yu, W. Guo, A. Zettl, H. Zheng, D. C. Chrzan and J. Wu, *Adv. Mater.*, 2015, **27**, 6841–6847.
64 X. Lu and C. Zhao, *Nat. Commun.*, 2015, **6**, 6616.
65 L. Yu, H. Zhou, J. Sun, F. Qin, F. Yu, J. Bao, Y. Yu, S. Chen and Z. Ren, *Energy Environ. Sci.*, 2017, **10**, 1820–1827.
66 J. Wang, F. Xu, H. Jin, Y. Chen and Y. Wang, *Adv. Mater.*, 2017, **29**, 1605838.
67 E. J. Popczun, J. R. McKone, C. G. Read, A. J. Biacchi, A. M. Wiltrout, N. S. Lewis and R. E. Schaak, *J. Am. Chem. Soc.*, 2013, **135**, 9267–9270.
68 N.-T. Suen, S.-F. Hung, Q. Quan, N. Zhang, Y.-J. Xu and H. M. Chen, *Chem. Soc. Rev.*, 2017, **46**, 337–365.
69 A. Oh, Y. J. Sa, H. Hwang, H. Baik, J. Kim, B. Kim, S. H. Joo and K. Lee, *Nanoscale*, 2016, **8**, 16379–16386.
70 T. Zhang, J. Du, P. Xi and C. Xu, *ACS Appl. Mater. Interfaces*, 2017, **9**, 362–370.
71 J. Yu, Q. Li, Y. Li, C.-Y. Xu, L. Zhen, V. P. Dravid and J. Wu, *Adv. Funct. Mater.*, 2016, **26**, 7644–7651.
72 G. F. Chen, T. Y. Ma, Z. Q. Liu, N. Li, Y. Z. Su, K. Davey and S. Z. Qiao, *Adv. Funct. Mater.*, 2016, **26**, 3314–3323.
73 A. Dutta, A. K. Samantara, S. K. Dutta, B. K. Jena and N. Pradhan, *ACS Energy Lett.*, 2016, **1**, 169–174.

74 J. Ryu, N. Jung, J. H. Jang, H.-J. Kim and S. J. Yoo, *ACS Catal.*, 2015, **5**, 4066–4074.
75 X. Yu, T. Hua, X. Liu, Z. Yan, P. Xu and P. Du, *ACS Appl. Mater. Interfaces*, 2014, **6**, 15395–15402.
76 D. Liu, Q. Lu, Y. Luo, X. Sun and A. M. Asiri, *Nanoscale*, 2015, **7**, 15122–15126.
77 J. W. Lee, T. Ahn, D. Soundararajan, J. M. Ko and J.-D. Kim, *Chem. Commun.*, 2011, **47**, 6305–6307.
78 M. Liu and J. Li, *ACS Appl. Mater. Interfaces*, 2016, **8**, 2158–2165.
79 J. Yu, Q. Li, Y. Li, C. Y. Xu, L. Zhen, V. P. Dravid and J. Wu, *Adv. Funct. Mater.*, 2016, **26**, 7644–7651.
80 X.-D. Wang, Y.-F. Xu, H.-S. Rao, W.-J. Xu, H.-Y. Chen, W.-X. Zhang, D.-B. Kuang and C.-Y. Su, *Energy Environ. Sci.*, 2016, **9**, 1468–1475.
81 S. Zhao, Y. Wang, J. Dong, C.-T. He, H. Yin, P. An, K. Zhao, X. Zhang, C. Gao and L. Zhang, *Nat. Energy*, 2016, **1**, 1–10.
82 J. Yang, G. Zhu, Y. Liu, J. Xia, Z. Ji, X. Shen and S. Wu, *Adv. Funct. Mater.*, 2016, **26**, 4712–4721.
83 J. Tian, N. Cheng, Q. Liu, X. Sun, Y. He and A. M. Asiri, *J. Mater. Chem. A*, 2015, **3**, 20056–20059.
84 Z. Yin, C. Zhu, C. Li, S. Zhang, X. Zhang and Y. Chen, *Nanoscale*, 2016, **8**, 19129–19138.